Reversible amorphous-crystalline phase changes in a wide range of Se1-xTex alloys studied using ultrafast differential scanning calorimetry

Vermeulen, Paul. A.; Momand, Jamo; Kooi, Bart J.

Published in:
Journal of Chemical Physics

DOI:
10.1063/1.4886185

Reversible amorphous-crystalline phase changes in a wide range of $Se_{1-x}Te_x$ alloys studied using ultrafast differential scanning calorimetry

Paul. A. Vermeulen, Jamo Momand, and Bart J. Kooi

Citation: The Journal of Chemical Physics **141**, 024502 (2014); doi: 10.1063/1.4886185
View online: https://doi.org/10.1063/1.4886185
View Table of Contents: http://aip.scitation.org/toc/jcp/141/2
Published by the American Institute of Physics

Reversible amorphous-crystalline phase changes in a wide range of $Se_{1-x}Te_x$ alloys studied using ultrafast differential scanning calorimetry

Paul. A. Vermeulen, Jamo Momand, and Bart J. Kooi[a)]
Zernike Institute for Advanced Materials, University of Groningen, Nijenborgh 4, 9747 AG Groningen, The Netherlands

(Received 24 March 2014; accepted 19 June 2014; published online 8 July 2014)

The reversible amorphous-crystalline phase change in a chalcogenide material, specifically the $Se_{1-x}Te_x$ alloy, has been investigated for the first time using ultrafast differential scanning calorimetry. Heating rates and cooling rates up to 5000 K/s were used. Repeated reversible amorphous-crystalline phase switching was achieved by consecutively melting, melt-quenching, and recrystallizing upon heating. Using a well-conditioned method, the composition of a single sample was allowed to shift slowly from 15 at. %Te to 60 at. %Te, eliminating sample-to-sample variability from the measurements. Using Energy Dispersive X-ray Spectroscopy composition analysis, the onset of melting for different Te-concentrations was confirmed to coincide with the literature solidus line, validating the use of the onset of melting T_m as a composition indicator. The glass transition T_g and crystallization temperature T_c could be determined accurately, allowing the construction of extended phase diagrams. It was found that T_m and T_g increase (but T_g/T_m decrease slightly) with increasing Te-concentration. Contrarily, the T_c decreases substantially, indicating that the amorphous phase becomes progressively unfavorable. This coincides well with the observation that the critical quench rate to prevent crystallization increases about three orders of magnitude with increasing Te concentration. Due to the employment of a large range of heating rates, non-Arrhenius behavior was detected, indicating that the undercooled liquid SeTe is a fragile liquid. The activation energy of crystallization was found to increase 0.5–0.6 eV when the Te concentration increases from 15 to 30 at. % Te, but it ceases to increase when approaching 50 at. % Te. © *2014 AIP Publishing LLC*. [http://dx.doi.org/10.1063/1.4886185]

I. INTRODUCTION

Phase transformations play a key role in material production, particularly of metals and polymers, but also in a large variety of natural processes.[1–5] Moreover, many advanced materials increasingly rely on controlled exploitation of phase transformations.[6–8] Polymers, alloys, polymorphic substances and composites develop a variety of structures, generally with a metastable nature, which depend on the cooling conditions during their production. During heating, reorganization processes such as (re)crystallization, phase separation and melting may occur. Differential Scanning Calorimetry (DSC) has been an important tool to study such processes. With the advent of ultrafast DSC heating and cooling rates of 10^4 K/s can be achieved. This has dramatically extended the application range of DSC.

In recent years, particularly polymers were studied using ultrafast DSC,[9–13] but also the application of this technique to so-called phase-change materials[14,15] has demonstrated its power to enter previously unexplorable analysis areas. Also, in the present work we apply this technique to a model-based phase-change material, in particular to study crystallization in SeTe chalcogenide alloys with a wide composition range.

Phase-change materials (PCMs) are currently investigated intensely, mainly to replace the popular Flash-type memory in the near future, which is used in, e.g., mobile phones, tablet computers, USB memory sticks.[8,16–18] PCMs already have been applied successfully in optical recording, well-known from the rewritable CD, DVD, and Blu-Ray Disk formats. Phase-change memories can be switched reversibly more than a million times between amorphous and crystalline states and exploit the large differences in optical reflectivity or electrical resistance of the two states.[8,16–18] A fast high energy pulse transforms the crystalline cell into an amorphous state by melt-quenching. The crystalline state can be re-obtained via a longer lower energy pulse that heats the cell optimally below the melting temperature, where the mobility of the atoms becomes high, allowing crystallization. This can be done fast (<100 ns), but not as fast as melt-quenching which is possible in picoseconds. Particularly, the combination of large electrical/optical property contrast with ultrafast crystallization kinetics at elevated temperatures required for fast switching, and ultraslow crystallization kinetics below 100 °C required for data retention is a unique feature of PCMs.[8,16–18]

Despite the interesting results obtained when ultrafast DSC was applied to the prototype $Ge_2Sb_2Te_5$ material,[14,15] the disadvantage of the analyses performed is that (i) only single (non-reversible) crystallization events could be monitored for thin film flakes deposited on the sensor and (ii) the PCM studied has an as-deposited structure, whereas melt-quenched structures are more relevant because they are exploited in all

a)Email: B.J.Kooi@rug.nl

memory applications. The usefulness of PCMs particularly originates from the reversible amorphous-crystalline phase transformation, where the amorphous phase is obtained by melt-quenching. This process was not studied with ultrafast DSC up to now and is the focus of the present work. We have selected a kind of model PCM, in fact SeTe alloys which allow (i) reversible phase switching by melting, melt-quenching into an amorphous phase and crystallization of this phase, (ii) precise control of the thermal history of the materials, and (iii) the execution of multiple measurements on single samples. Such an analysis of PCMs is aimed to provide deeper insights in the extraordinary phase transformation kinetics of these materials excellently suited for data storage applications.

II. MATERIALS AND METHODS

Several $Se_{1-x}Te_x$ alloys with x = (15; 25; 50) were prepared by adding for each of them appropriate amounts of the pure constituents (99.999% purity) to a quartz ampoule. The ampoule was brought under vacuum and sealed. The alloy was then left in an oven at 400 °C (which is well above melting point of the alloy) for at least 16 h. The ampoule was then slowly cooled down to room temperature. Using Energy Dispersive X-ray Spectrometry (EDXS), connected to a Scanning Electron Microscope (SEM) it was verified that the ingot was completely homogeneous. A flake of the alloy was placed on the DSC sensor using a hair.

When the flake was deposited on the sample area of the sensor, it was generally in poor contact with the sample area. Melting the flake, creating a droplet-shaped sample, resulted in a very good contact with the sensor surface (see supplementary material,[41] Secs. 1 and 2). Moreover, each time the sample is molten during the reversible phase switching any previous thermal history is erased.

Based on microscopy observations, including for various samples detailed SEM images (see, e.g., Figs. S8 and S13 in the supplementary material[41]), the (top view) diameters for initially molten flakes were determined and varied between 70 and 150 μm for different SeTe samples. Due to evaporation the volume of the droplets reduces during the experimental sequence we pursued and therefore an appropriate average value is 100 μm. The volume of the droplet can be approximated well by a hemisphere and therefore its height is about 50 μm. Using the densities of solid Se (4.8 g cm^{-3}) and Te (6.2 g cm^{-3}) the sample mass is in the range 1–2 μg.

The ultrafast DSC used in this research was a Mettler Toledo Flash DSC 1, with the UFS-1 sensor chip containing the actual DSC sensor- and reference-crucibles.[19] During all measurements, the volume around the sensor area was flushed with nitrogen (20 ml/min), preventing oxidation and ensuring constant environmental conditions. The sensor surroundings were kept at −90 °C by an intercooler.

The aim to reversibly switch a chalcogenide-based PCM using melt-quenching is still clearly limited by the maximum achievable temperature of the UFS-1 sensor, which is about 450 °C and its maximum cooling rate of about 5000 K/s. Therefore, the SeTe alloy was selected, because of its low melting temperatures (325 °C for 50% Te, see Fig. 2) and because it is known from literature that the alloy is easily vitrified below 30 at. % Te.[20–22] Particularly, this last property is not really representative for PCMs exploited for memory application, because they are generally poor glass formers requiring much higher cooling rates than possible in the Flash DSC, but these rates are readily achieved using nanosecond laser or electrical pulses. Nevertheless, the SeTe alloy allows for the first time the study of the reversible amorphous-crystalline phase change in a chalcogenide material using ultrafast DSC.

In our measurement method we particularly used the Flash DSC for its ability to quickly melt-quench the material and thus obtain vitrified SeTe alloys as starting point for consecutively heating runs allowing crystallization with various heating rates. The heating rates we applied were relatively low, in general between 1 and 1000 K/s, clearly less than the capability of the Flash DSC to heat with 40 000 K/s. The reason we limited the heating rates was to ensure that thermal lag effects, e.g., due to thermal gradients in our sample, remained small and therefore did not significantly affect our measurement results. In the supplementary material (Secs. 1 and 2)[41] we demonstrate by experimental calibration and by detailed thermal analysis that lag effects indeed remain small in our samples for heating rates up to 1000 K/s.

As will be shown below a general measurement typically consists of a sequence of various heating rates only to a limited temperature beyond the one of the crystallization peaks of SeTe. For higher temperatures including the melting of SeTe all heating was typically performed at a rate equal to the maximum rate in the sequence, but not higher than 200 K/s. The reason for this switching in heating rate beyond the crystallization peak will become clear from the experimental results below, where particularly the time spent at the highest temperatures is minimized in order to minimize evaporation of the SeTe samples.

III. RESULTS AND DISCUSSION

A typical DSC measurement sequence on a single sample (starting composition $Se_{85}Te_{15}$) is shown in Fig. 1(a). Four DSC curves have been recorded using various heating rates (3, 5, 8, 10 K/s), the quench rate was kept prior and in-between the heating steps constant at −4000 K/s. At 200 °C the heating rates of 3, 5, and 8 K/s were switched to 10 K/s, to ensure the melting of the sample was measured for these four cases at the same heating rate. This reduced the influence of variations in thermal lag on the measured melting point. Furthermore, it ensured the alloy was in the molten state for the same short amount of time for each measurement. The glass transition T_g, crystallization peak temperature T_c, and onset of melting T_m, are clearly observable in Fig. 1(a) and this was observed in general for all heating rates.

In Fig. 1(b) results at relatively higher heating rates for a different sample (starting composition $Se_{75}Te_{25}$) are shown for the same prior melt-quench rate of −4000 K/s. Since heat capacity is measured the glass transition should appear as a step (although complications can arise due to under- or overshoots[23] and for the Flash DSC also due to one-sided heat losses to the cold nitrogen environment) where its midpoint

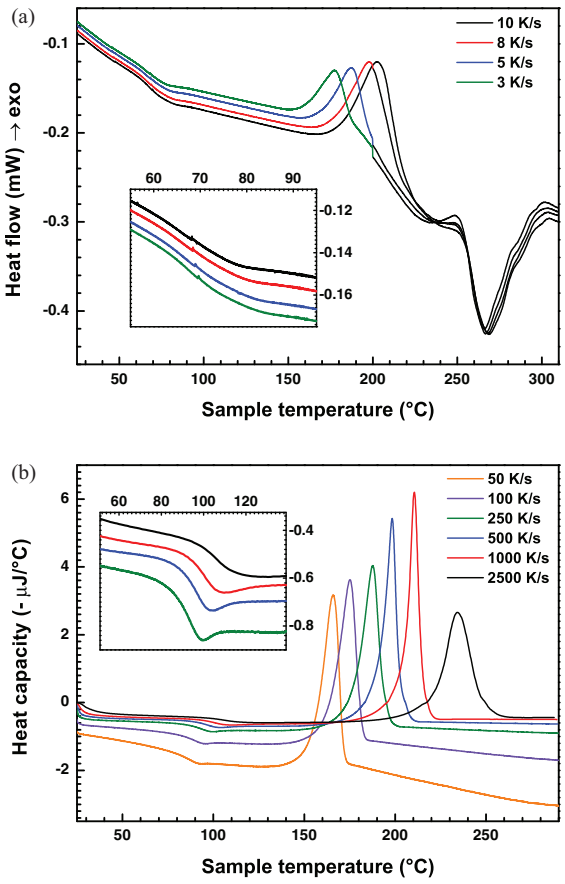

FIG. 1. (a) A typical set of DSC curves obtained during heating at various rates (from lowest to highest T_c peak temperature: 3, 5, 8, 10 K/s) of a SeTe alloy that was quenched from the liquid state (320 °C) at a rate of −4000 K/s. The heat flow to the sample crucible is plotted versus the sample temperature. A peak indicates an exothermic process. The glass transition T_g, crystallization peak T_c, and the onset of melting T_m have been obtained using an algorithm to find the tangents to the curve. The inset shows an enlargement of the glass transition region that can be compared with the one in Fig. 1(b). The heating rate between 25 °C and 200 °C is varied. From 200 °C to 320 °C, the heating rate is kept constant at 10 K/s. (b) A typical set of DSC curves obtained at higher heating rates than in (a) with now heat flow divided by heating rate such that a measure of heat capacity C_p is plotted along the vertical scale. Quench rate was kept at −4000 K/s. Clear evolution in behavior of the glass transition as a function of heating can be observed that is highlighted in the inset. Also a clear evolution in the crystallization peaks can be discerned. Both these evolutions are explained in the main text.

in heat flow generally can be taken as representative for the glass transition temperature T_g. Effectively the same result is obtained when two temperatures are identified, corresponding to changing slopes in the recorded curves, that signify the beginning and ending of the glass transition, where T_g is defined as their average (in compliance with the ASTM E1356 standard). In Fig. 1(b) it can be observed that, when the heating rate (e.g., 2500 K/s) approaches the prior cooling rate of 4000 K/s, indeed the glass transition occurs by a well-defined step. However, when the heating rate becomes progressively lower than the prior cooling rate the step becomes increasingly distorted due to two reasons: (i) in the Flash DSC only one side of the sample is heated while the other side is in contact with flowing nitrogen in addition to the cold surrounding which is kept at −90 °C; (ii) undershoots develop in accordance with theoretical and experimental expectations.[23] In Fig. 1 the effect (i) is dominating below about 50 K/s as can also be observed by the differences in slope, i.e., heat loss for the SeTe glass, undercooled liquid, and crystalline state. The lower the heating rate the steeper the slopes in general become. In the crystalline state the SeTe conduct heats better than in the glassy state and in the undercooled liquid the heat conduction is lowest. Therefore, at the lowest heating rates the negative slope in Fig. 1 is steepest for the crystalline state, somewhat less steep for the glassy state and least (most horizontal) for the undercooled liquid. As a consequence at the lowest heating rates the glass transition, instead of a step, becomes nearly a kink. This can be observed clearly in Fig. 1(a) and the gradual development from a step to this kink can be clearly observed in Fig. 1(b).

Another issue is that it can be debated whether T_g can be measured correctly during heating, since it can be argued that T_g is only determined correctly upon cooling from the equilibrium state.[23] In that sense our reference to T_g in the remainder of this paper should be taken as a reference to a representative (near fictive) temperature directly associated with the glass transition process but not the glass transition temperature in a strict sense.

The crystallization temperature T_c is taken as the temperature where the peak of crystallization occurs (cf. Figs. 1(a) and 1(b)). The peak temperature is taken, because it coincides with the maximum in the reaction rate, which is required for the Kissinger analysis.[24] A clear systematic trend in the evolution of the crystallization peak as a function of heating rate can be observed in Fig. 1(b) for the range 50 to 1000 K/s. However, increasing the heating rate (beyond 1000 K/s) to 2500 K/s results in a strong deviation of this trend with a considerable broadening of the crystallization peak and thus lowering of its maximum. This effect can be attributed to considerable thermal lag due to thermal gradients in the amorphous droplet-shaped sample for heating rates well beyond 1000 K/s and relatively insignificant lags for heating rates of 1000 K/s or lower. This observation agrees well with our detailed analysis of thermal lag performed in Sec. 1 of the supplementary material.[41]

Finally, the melting point T_m is defined as the onset of the melting peak. The onset is defined as the intersection point of the baseline of the DSC curve and steepest tangent to the melting peak. To reduce measurement noise, all raw curves were processed with a Savitzky-Golay filter.[25]

The DSC curves such as displayed in Fig. 1 demonstrate that the SeTe alloy can be switched reversibly between the amorphous and crystalline phases by a melt-quench technique using ultrafast DSC. After the melt-quenching, the T_g, T_c, and T_m can be clearly distinguished during heating.

Due to the open structure of the UFS-1 sensor, sample material evaporated from the sensor area when heated to the higher temperatures. This material for a large part precipitated on the cold area around the sensor, creating a halo of SeTe around the heated sample area (see Fig. S8 in the supplementary material where the halo can be clearly observed in a SEM image[41]). This mass loss effect could also be seen directly from DSC analysis, since the area of the melting peak reduced slightly in each subsequent measurement (see Fig. S9 in the supplementary material[41]). The sample environment will never be saturated with gaseous selenium or

tellurium because the evaporated material is removed almost immediately from the surroundings by precipitation and flushing, causing the sample to continuously lose mass.

Accompanying the sample mass reduction, the melting temperature T_m was also found to increase slightly with each heating run. This indicated a decreased Se/Te ratio, due to disproportionate evaporation of selenium from the alloy. This can be readily explained by noting the different vapor pressures of selenium and tellurium.[26] The higher vapor pressure (lower melting and boiling points) of selenium indicates that a larger driving force for evaporation is present. These evaporation effects were directly proportional to the time spent at high temperatures and therefore we used in general measurement sequences minimizing this time.

To investigate this composition shift of the alloy, and the connection between composition and the measured melting point, several samples with different melting temperatures were investigated using a SEM combined with EDXS. These measurements were conducted for several different UFS-1 sensors and SeTe alloy droplets, to account for sample variability. By plotting the (EDXS) measured atomic composition against the T_m as measured with ultrafast DSC, a phase diagram was constructed, see Fig. 2, relating the melting point of the alloy to its composition. Fig. 2 shows a very good agreement between EDXS combined with ultrafast DSC measurements and literature, validating the use of the onset of melting as a direct measure of the Te concentration. This onset of melting was therefore used to determine the composition of the alloy for each measurement sequence, making it unnecessary to check composition with EDXS after each heating run.

The fact that the sample size decreases with each run as Se preferentially evaporates is not negatively affecting our results, because the sample is generally completely molten after each run and therefore the thermal contact and composition will be reformed each run. In this respect there is in principle no difference whether for a certain composition the sample is molten for the first time or many times. Of course, only when a sample tends to be largely evaporated, the measurement accuracy deteriorates due to the reduction of the signal to noise ratio. An advantage of the evaporation initially is that the sample size reduces, where particularly the reduction in sample height reduces the potential thermal gradients in the sample and thus increases accuracy.

Using a quench rate of −4000 K/s, it was possible to quench SeTe alloys up to at least 40 at. % Te to the amorphous state without an observable crystallization peak during cooling. In the range from ∼40–60 at. % Te an increasing fraction of the material crystallizes upon cooling at −4000 K/s and this fraction becomes 100% beyond ∼60 at. % Te. These observations agree with the literature, stating pure Te as a crystalline and pure Se as an amorphous (vitreous) material. The melting temperature is that of a nearly perfectly mixed alloy and therefore is approximately a linear interpolation between the melting points of the pure constituents.[20]

Extended phase diagrams have been constructed for three samples, and are shown in Figs. S10 and S11 of the supplementary material.[41] Combined information of two different samples, showing the consistency of the results and the validity of our methodology (reproducible reversibility with gradual decrease in Se concentration), is shown in Fig. 3. The diagrams show T_c and T_g (obtained during heating after the quenching) for various heating rates, as well as the melting temperatures T_m. The results in Fig. 3 below 30 at. % Te are obtained from (Fig. S10(a) for) a sample with starting composition $Se_{85}Te_{15}$ and above 30 at. % Te from (Fig. S11 for) a sample with starting composition one with $Se_{75}Te_{25}$. In fact, continuously repeating measurement sequences shown in Fig. 1(a) allowed the construction of the results below 30 at. % Te in Fig. 3 (and all results in Fig. S10(a)). The same holds for Fig. 1(b) and the results above 30 at. % Te in Fig. 3 (or Fig. S11, where in Fig. 1(b) only a limited number of heating rates of the actual sequence were shown to improve visibility).

The extended phase diagrams show clear evolutions of the transition temperatures with Te concentration. A decreasing T_c is observed for increasing at. % Te, while T_g

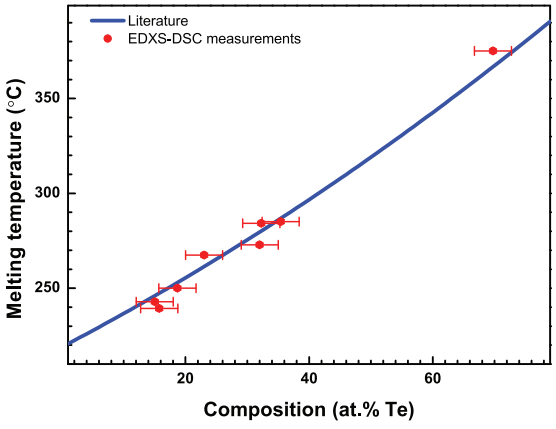

FIG. 2. The atomic composition of the SeTe alloy was measured using EDXS, and plotted against the onset of melting as measured by the ultrafast DSC. These points are displayed in red. The blue line is taken from literature (see Ref. 20, and references therein). The experimental results agree well with literature.

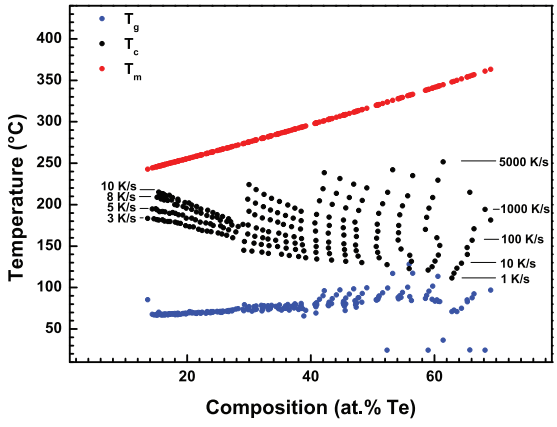

FIG. 3. Extended phase diagram showing as a function of Te concentration the glass transition temperature T_g, crystallization temperatures T_c and melting temperatures T_m. Particularly T_c increases for increasing heating rates; this increase is more pronounced for relatively low Te concentrations. T_c decreases and T_g increases with increasing Te concentration. The data points at the highest Te concentrations, beyond 60 at. % Te, are inaccurate due to too low quench rate for complete amorphization and due to severe mass loss in the sample as caused by evaporation.

increases slightly for increasing at. % Te. When the heating rate is increased, a significant increase in T_c is observed. This can be explained by recognizing that crystallization is a thermally activated process. When the material is heated at a higher rate, less time has passed at a certain temperature. This means the material has had less time to nucleate and grow. Therefore, the maximum growth rate occurs at higher temperature.

Increasing the heating rate also increases T_g, but the effect for T_c is clearly more pronounced. In Fig. 3 the difference between the T_c's pertaining to the lowest and highest heating rates decreases with increasing Te concentration. This indicates (based on Kissinger analysis[24]) that the activation energy for crystallization increases with increasing Te concentration. In Fig. 3 it seems that, by extrapolating the observed trends in the data below 40 at. % Te to higher Te concentration, the activation energy for crystallization tends to diverge (become infinite) when the crystallization temperature becomes independent of heating rate, i.e., when straight lines fitted to the data for the various heating rates converge and finally cross when extrapolated to higher Te concentration (see also Fig. S10 in the supplemetary material[41]). Moreover, this crossing tends to occur when the crystallization temperature also approaches the glass temperature at Te concentrations of about 70–80 at. % Te. However, Fig. 3 shows that one has to be careful with drawing conclusions from such extrapolations, because it indicates that beyond ∼50 at. % Te, the activation energy for crystallization is not increasing further.

Still, the results in Fig. 3 prove that the gap between the glass temperature and the crystallization temperature (observed for a certain heating rate, particularly the lowest heating rate), i.e., a kind of overheating, rapidly decreases for increasing Te concentration (in the range up to 60 at. % Te) by a slight increase of the glass temperature, but particularly by a pronounced decrease in crystallization temperature. Simultaneously the gap between the melting temperature and the crystallization temperature, i.e., a kind of undercooling, rapidly increases by both a pronounced increase of the melting temperature and a pronounced decrease in crystallization temperature. These results thus clearly show that the glass-forming ability of SeTe alloys continuously and strongly decreases in the range from 15 to 60 at. % Te.

The reduced glass temperature ($T_{rg} = T_g/T_m$) shows a slow decrease with increasing Te concentration; approximately 0.66 at 15 at. % Te to 0.60 at 50 at. % Te. This does not really seem significant compared to the change in T_c. However, interestingly this observed decrease in T_{rg} agrees with the expectation (see, e.g., Ref. 27) that T_{rg} decreases when the glass-forming ability decreases.

In Fig. 4 the critical quench rate (QR_{crit}) necessary to completely vitrify the sample is shown. This rate was determined by the lowest tested rate where a crystallization peak was not detected upon cooling the sample. It is found that this rate increases orders of magnitude from 10 K/s for ∼20 at. % Te to 6000 K/s for ∼60 at. % Te. Of course the QR_{crit} is a direct measure of the glass-forming ability and thus also demonstrates that this ability strongly decreases in the range from 15 to 60 at. % Te. From the critical quench rates shown in Fig. 4, we can deduce that the temperature gap between T_c and T_m shown in Fig. 3 is an important indicator for the quench rate needed to prevent crystallization, since a lower T_c means an increased driving force for crystallization due to the increased undercooling. This means that as the tellurium concentration increases, the quench rate necessary to vitrify the sample needs to be increased, to counterbalance the increased driving force of crystallization.

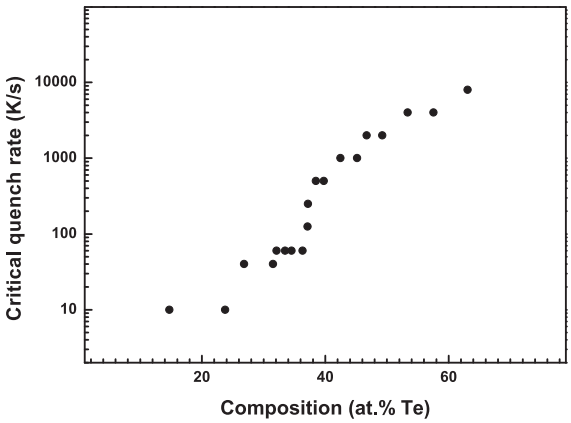

FIG. 4. Critical melt-quench rate to achieve the amorphous phase without any observable crystallization during cooling as a function of Te concentration. The critical rate increases orders of magnitude from 10 K/s at ∼20 at. % Te to 6000 K/s at ∼60 at. % Te.

By varying the quench rate and measuring T_c, it was found that the quench rate does not significantly influence the crystallization temperature T_c (see Fig. S12 in the supplementary material[41]). When crystallization is strongly limited by nucleation, then it is expected that at the lowest quench rates more embryos for nucleation can develop than at the highest quench rates and then a significant decrease in crystallization temperature upon heating is expected after the lowest quench rates. Since, this effect is not observed, it can be concluded that crystallization is not limited by nucleation, but predominantly by growth. This is also corroborated by the observations that the trend in crystallization temperature versus Te concentration does not change when the sample is not fully vitrified anymore after quenching and thus already contains a crystalline fraction either due to incomplete melting of the crystalline material or due to partial crystallization during quenching.

Kissinger analysis[24] was applied to the crystallization transition to determine the activation energy (E_c), i.e., data plotted in a graph of $\ln(\phi/T_c^2)$ versus $(1/T_c)$ should be on a straight line with a slope equal to $(-E_c/k_B)$, with ϕ the heating rate, T_c the crystallization peak temperature, k_B Boltzmann's constant, and E_c the activation energy for crystallization.

Since Kissinger analysis enables the determination of the activation energy of a certain alloy, the composition must not change significantly between heating runs. Fig. 1(a) demonstrates that the composition shift within one measurement sequence can be minimized to less than 2 at. % (since the onset of melting of the four sequential heating curves does not show an observable shift). Furthermore, from Fig. 3 the maximum composition difference observed within a measurement sequence is 2.5 at. % Te. These composition shifts are

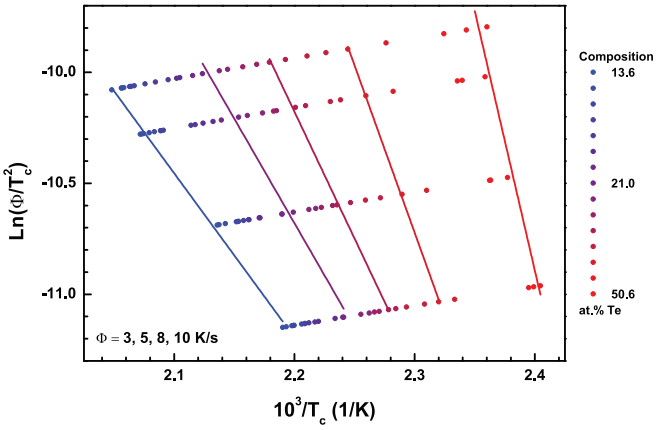

FIG. 5. A Kissinger plot showing the crystallization peaks of all SeTe compositions during the extended analysis of a single sample. The composition is denoted by color, with low Te-concentrations in blue, progressing to red for higher Te-concentrations. A linear fit is made through four measurements of one sequence, with different heating rate (in this case 3, 5, 8, 10 K/s) for approximately the same composition. From these fits, the activation energy for crystallization at one alloy composition was obtained. A few fitted lines are shown as a guide to the eye. The slope of the lines clearly increases as the Te concentration increases.

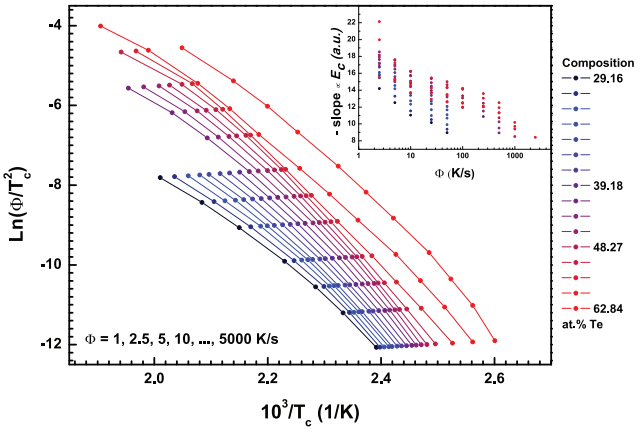

FIG. 6. A Kissinger plot showing the crystallization peaks of all SeTe compositions during the extended analysis of a single sample. The composition is denoted by color, with low Te-concentrations in blue, progressing to red for higher Te-concentrations. The lines connect the points with different heating rates (for lowest concentrations: 1, 2.5, 5, 10, 25, 50, 100 K/s; adding 250, 500, 1000 K/s data points for the next step, next 2000 K/s and even for the highest point 5000 K/s. A clear curvature is visible in the trend presented by the data. Furthermore, the overall slope becomes steeper as the Te concentration increases. The inset shows the negative of the local slope (since this is proportional to activation energy) of each series as a function of heating rate ϕ. A linear fit is made through three points to obtain these slopes. It is clear that the slope steepness decreases as the heating rate increases, giving a measure of curvature. The inset also shows that the slopes increase for higher Te concentration.

considered to be sufficiently small, allowing the Kissinger analyses to be performed with sufficient accuracy.

The Kissinger plot shown in Fig. 5, which connects the T_c measurements of one sequence like the one shown in Fig. 1(a), allows determination of the slope from a least-squares fit. All data points are colored coded based on their composition. The plot shows the slopes of a few fits, as a guide to the eye. The slopes of the fitted lines slowly become steeper for an increasing tellurium concentration and therefore the activation energy E_c increases with increasing Te concentrations. The data points show a good compliance with the linear fitted trends, although increased errors are observed for higher Te concentrations. Due to sample mass reduction through evaporation the DSC curve signal/noise ratio decreases as the sample has been through more heating runs and therefore the increase in error can be anticipated. However, an important other source of error is that beyond 30 at. % Te the melting was not performed at sufficiently high temperature (sufficiently long time) to fully melt the crystallized material (see Fig. S13 in the supplementary material[41]). Therefore, beyond 30 at. % Te only part of the sample is vitrified during quenching and this leads to more variations in the results. The same was actually true for the data beyond 30 at. % Te in Fig. S10(a) and therefore we used only the data below 30 at. % of this sample for the construction of Fig. 3. Still, the continuous trend in results below and above 30 at. % Te in Fig. 5 (and Fig. S10(a) of the supplementary material[41]) indicates that results are not sensitively depending on complete absence of prior crystallization.

Compared to Fig. 5, Fig. 6 depicts a Kissinger plot that connects the T_c measurements for a much wider range of heating rates, particularly also employing higher heating rates of which examples are shown in Fig. 1(b). The data in this plot show a clear curvature. This curvature is illustrated by the inset, which shows the local slope of all points in the Kissinger plot. The slope clearly lowers for higher heating rates, regardless of the composition. From lag characterization measurements and from a detailed thermal analysis (see supplementary material, Secs. 1 and 2[41]) it is determined that the lag at heating rates of 1000 K/s is less than 4 K (in agreement with earlier work[28]). It is therefore insufficient to explain the measured curvature, which is also observable for heating rates up to 1000 K/s. Therefore, the curvature is related to the crystallization process in the SeTe alloy itself. This non-Arrhenius behavior can readily be attributed to fragile liquid behavior of the SeTe undercooled liquid. A seminal paper of Martinez and Angell[29] already shows that Se exhibits significant fragility. In that respect our observation of fragility in SeTe alloys might be expected and is thus corroborated by the experimental results here. A similar non-Arrhenius behavior effect was found in the study of $Ge_2Sb_2Te_5$,[14] where ultrafast DSC was also used to produce data in a Kissinger plot with heating rates up to $4*10^4$ K/s. There the non-Arrhenius behavior was also attributed to fragile liquid behavior ($m \approx 90$ whereas $m \approx 15$ for strong liquid behavior). In a recent paper on GeTe it was also concluded that the undercooled liquid has a high fragility with at least a value $m \approx 130$.[30] Fig. 6 seems to indicate that fragility reduces with increasing Te concentration, because curvature is most pronounced for alloys containing least Te.

As already shown above, the crystallization rate in SeTe is predominantly governed by crystal growth (and not limited by crystal nucleation). Crystal growth is, for the temperature regime considered here for the Kissinger plot at relatively large undercoolings, governed by the microscopic atomic mobilities of the undercooled liquid. These mobilities are, according to the Stokes-Einstein relation, inversely proportional to the macroscopic viscosity η. We are certain that we have an

undercooled liquid, because our measurements demonstrate that we are above the glass transition temperature. The activation energy of the (overall) crystallization process in SeTe, as can be derived from the Kissinger plot, is thus directly related to the temperature dependence of the viscosity. For a strong liquid this temperature dependence is of Arrhenius type. For a fragile liquid this temperature dependence would indicate that the local slope in the Kissinger plot decreases for increasing peak temperatures and thus for increasing heating rates, exactly what is observed in Fig. 6. Therefore, it is clear that the Kissinger plot in Fig. 6 is consistent with fragile liquid behavior.

Moreover, the inset in Fig. 6 demonstrates that the local slope in the Kissinger plot becomes steeper for increasing Te concentration, meaning that the activation energy E_c increases with increasing Te concentration. This holds in general for all heating rates.

Based on the results such as obtained from Figs. 5 and 6 (where from Fig. 5 only the results below 30 at. % Te were incorporated, because of incomplete melting of the sample beyond 30 at. % Te), Fig. 7 is constructed showing the obtained activation energy E_c as a function of Te concentration for three independent samples. The activation energies were also determined using the Ozawa method,[31,32] yielding similar activation energies, to within 2% of the values obtained using Kissinger analysis. In Fig. 7, each point represents the activation energy obtained from the linear fit of all points of the same composition, such as displayed in Figs. 5 and 6, neglecting curvature effects which, as shown above, become more pronounced when higher heating rates are included.

Fig. 7 shows that the range of heating rates, particularly the highest heating rates, affects the values obtained for the activation energy E_c. An important factor explaining this trend is the curvature in the Kissinger plot shown in Fig. 6. If the curvature is neglected to fit the data linearly, the calculated slope will be too flat and E_c thus too low. This error will increase when the range in heating rate, particularly the maximum heating rate is increased. It explains why the heating rate ranges with maximum values of 100 and 1000 K/s in Fig. 7 tend to give systematically lower values for E_c than the ones for the lower maximum heating rates, because fragility of the supercooled liquid leads to curvature in the Kissinger plot. However, on top of the curvature effect due to fragility, the heating rate ranges with maximum values of 2500 and 5000 K/s become even more curved due to thermal lag effects and therefore give relatively even lower values for the activation energy E_c. Despite this (obscuring) influence of heating rate range, also the influence of Te concentration on the activation energy E_c can still be observed well in Fig. 7. It shows that the increase in activation energy as a function of Te concentration is most pronounced for 15–30 at. % Te and gradually reduces with increasing Te concentration. Finally, the increase in E_c tends to disappear beyond about 50 at. % Te.

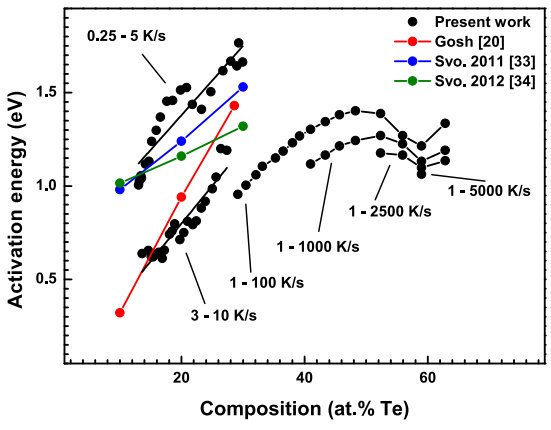

FIG. 7. The activation energy of crystallization of various SeTe alloys (as obtained through Kissinger analysis) is plotted as a function of alloy composition. Results of three samples are shown, which have been tested in various ranges of heating rates. Literature values[20,33,34] have been plotted as well, showing fair agreement with the data of our present work. The solid lines represent linear fits as a guide to the eye. Explanations of some systematic trends in the data with heating rate ranges and Te concentration and also the effect of sample-to-sample variation are given in the main text of the article.

However, curvature effects in the Kissinger plot cannot explain the large difference in the activation energy observed between the heating rate ranges 0.25–5 K/s and 3–10 K/s. Several literature values[20,33,34] are plotted as well in Fig. 7, where particularly the results of Gosh *et al.*[20] show fair agreement with our data measured in the range 3–10 K/s, whereas the results of Svoboda *et al.*[33] agree better with our data measured in the range 0.25–5 K/s. Moreover, in Fig. S14 of the supplementary material[41] we show results for a total of seven different samples (instead of 3 different ones in Fig. 7), where the various trends are less clear than in Fig. 7, but demonstrating better that there is quite some sample-to-sample variation. However, still a similar trend is observed for various samples in Fig. S14, even though they show relatively large differences in the ordinate values. This trend indicates that there is an increase of 0.5–0.6 eV in the activation energy of crystallization when the Te concentration increases from 15–30 at. %. So, the relative large differences observed for the activation energy of crystallization in literature is reproduced here as sample-to-sample variations particularly giving various offset values in the activation energy. Therefore, it is relevant to try to find possible origins of these sample-to-sample variations in the absolute values of the activation energies.

We first need to recognize that the activation energy determined is an overall activation energy. It does not directly give us the energy barrier atoms need to overcome to allow the transition from the amorphous to crystalline phase, but it is the result of the contributions of both nucleating and growing crystals in various configurations. Due to the differences in sample mass and geometry, samples might show slightly different crystallization characteristics, where different crystallization mechanisms and also different crystal structures can be involved. A variable which was not well-controlled was the sample size. A bigger sample has a relatively low surface area compared to the bulk. This might lead to another crystallization regime.[34–37] Moreover, SeTe and even pure Se are characterized by a relatively large variety of allotropes that can develop.[38–40] Nucleation and growth processes for these different structures will vary and will thus also show variations in their activation energies. These results clearly indicate the importance to be able to perform repetitive measurements on single samples in order to observe trends that cannot be

detected otherwise due to sample-to-sample variation. This clearly shows the importance of the present methodology to be able to reversible switch the samples in an ultrafast DSC.

An increase in activation energy for increased Te concentration has been observed, while the crystallization temperature decreases. This might at first glance seem counter intuitive, but it shows that the difference in Gibbs free energy (ΔG) between the amorphous and the crystalline phases increases relatively faster than the activation energy for crystallization E_c increases in order to compensate for the observed increase of E_c.

IV. CONCLUSIONS

A reversible amorphous-crystalline phase change in a chalcogenide material has been investigated for the first time using ultrafast DSC. SeTe alloys with a concentration in the range between 15 and about 60 at. % were switched reversibly between the amorphous and crystalline phases. Using a quench rate of −4000 K/s, it was possible to quench SeTe alloys up to at least 40 at. % Te to the amorphous state without an observable crystallization peak during cooling. The ultrafast DSC measurements showed good signal/noise ratio and allowed for accurate determination of the glass transition temperature T_g, crystallization temperature T_c, and melting point T_m upon heating of the quenched materials.

The SeTe alloys slowly evaporated from the sensor. EDXS showed that the composition slowly shifted to higher Te-concentrations. It was proven using EDXS-DSC that the onset of melting measured by the ultrafast DSC is a good indicator of composition for this system. The slow shift in composition allowed for the scanning of crystallization behavior throughout a range of compositions (15–60 at. % Te). Using the observed transition temperatures T_g, T_c, and T_m as a function of Te concentration our measurement methodology allowed us to construct an extended phase diagram. T_c and T_g increase for increased heating rates. T_g increases slowly with increasing Te-concentration. However, the reduced glass temperature slowly decreases. The crystallization temperature on heating is found to decrease substantially with increasing Te concentration. Together with the significant increase in melting temperature, this is a strong signature that the amorphous phase becomes progressively unfavorable (with respect to the crystalline phase), which is of course excellently corroborated by our measurement that the critical quench rate, necessary to completely vitrify the sample, increases about three orders of magnitude (from ∼10 to ∼10 000 K/s) when the Te concentration increases from 20 to 60 at. %.

Kissinger and Ozawa analyses were performed to determine the activation energies of crystallization of the SeTe alloys. The capability of ultrafast DSC to exploit a large heating range enabled detection of non-Arrhenius behavior that can be attributed to fragile liquid behavior of the SeTe undercooled liquid. The activation energy of crystallization was found to increase for increased Te-concentrations; 0.5–0.6 eV when Te concentration increases from 15 to 30 at. %. However, the absolute values of the activation energy for crystallization differed considerably from sample-to-sample. Some potential origins for these differences have been highlighted.

ACKNOWLEDGMENTS

This work was in part supported by the EU within the FP7 Project PASTRY (GA 317746).

[1] *Phase Transitions in the Early Universe: Theory and Observations*, NATO Science Series, II Mathematics, Physics and Chemistry Vol. 40, edited by Héctor J. Vega, Isaak Markovich Khalatnikov, and Norma Sánchez (Kluwer Academic Publishers, 2001).
[2] S. Labrosse, J. W. Hernlund, and N. Coltice, Nature **450**, 866–869 (2007).
[3] M. Matsumoto, S. Saito, and I. Ohmine, Nature **416**, 409–413 (2002); R. McGraw and Y. Liu, Phys. Rev. Lett. **90**, 018501 (2003).
[4] D. A. Porter and K. E. Easterling, *Phase Transformations in Metals and Alloys*, 2nd ed. (CRC Press, 2004).
[5] S. Z. Cheng, *Phase Transitions in Polymers: The Role of Metastable States*, 2nd ed. (Elsevier Science, 2008).
[6] B. C. De Cooman, Curr. Opin. Solid State Mater. Sci. **8**, 285–303 (2004).
[7] R. Kainuma, Y. Imano, W. Ito, Y. Sutou, H. Morito, S. Okamoto, O. Kitakami, K. Oikawa, A. Fujita, T. Kanomata, and K. Ishida, Nature **439**, 957–960 (2006); M. Behl, M. Y. Razzaq, and A. Lendlein, Adv. Mater. **22**, 3388–3410 (2010).
[8] M. Wuttig and N. Yamada, Nat. Mater. **6**, 824–832 (2007).
[9] I. Kolesov, D. Mileva, R. Androsch, and C. Schick, Polymer (Guildf). **52**, 5156–5165 (2011).
[10] D. Zohrabyan, B. Milkereit, O. Kessler, and C. Schick, Thermochim. Acta **529**, 51–58 (2012).
[11] A. Wurm, E. Zhuravlev, and K. Eckstein, Macromolecules **45**, 3816–3828 (2012).
[12] M. van Drongelen, T. B. van Erp, and G. W. M. Peters, Polymer (Guildf). **53**, 4758–4769 (2012).
[13] R. T. Tol, A. A. Minakov, S. A. Adamovsky, V. B. F. Mathot, and C. Schick, Polymer (Guildf). **47**, 2172–2178 (2006).
[14] J. Orava, A. L. Greer, B. Gholipour, D. W. Hewak, and C. E. Smith, Nat. Mater. **11**, 279–283 (2012).
[15] J. Orava, A. L. Greer, B. Gholipour, D. W. Hewak, and C. E. Smith, Appl. Phys. Lett. **101**, 091906 (2012).
[16] D. Lencer, M. Salinga, and M. Wuttig, Adv. Mater. **23**, 2030–2058 (2011).
[17] S. Raoux, Annu. Rev. Mater. Res. **39**, 25–48 (2009).
[18] G. W. Burr, M. J. Breitwisch, M. Franceschini, D. Garetto, K. Gopalakrishnan, B. Jackson, B. Kurdi, C. Lam, L. A. Lastras, A. Padilla, B. Rajendran, S. Raoux, and R. S. Shenoy, J. Vac. Sci. Technol., B: Microelectron. Nanometer Struct. **28**, 223 (2010).
[19] S. van Herwaarden, E. Iervolino, F. van Herwaarden, T. Wijffels, A. Leenaers, and V. Mathot, Thermochim. Acta **522**, 46–52 (2011).
[20] G. Ghosh, R. C. Sharma, D. T. Li, and Y. A. Chang, J. Phase Equilibria **15**, 213–224 (1994).
[21] B. Bureau, S. Danto, H. L. Ma, C. Boussard-Plédel, X. H. Zhang, and J. Lucas, Solid State Sci. **10**, 427–433 (2008).
[22] B. Bureau, C. Boussard-Pledel, P. Lucas, X. Zhang, and J. Lucas, Molecules **14**, 4337–4350 (2009).
[23] P. Badrinarayanan, W. Zheng, Q. Li, and S. L. Simon, J. Non-Cryst. Solids **353**, 2603–2612 (2007).
[24] H. E. Kissinger, Anal. Chem. **29**, 1702–1706 (1957).
[25] A. Savitzky and M. Golay, Anal. Chem. **36**, 1627–1639 (1964).
[26] L. S. Brooks, J. Am. Chem. Soc. **74**, 227–229 (1952).
[27] W. Xu, L. M. Wang, R. A. Nieman, and C. A. Angell, J. Phys. Chem. B **107**, 11749–11756 (2003).
[28] G. Vanden Poel, D. Istrate, A. Magon, and V. Mathot, J. Therm. Anal. Calorim. **110**, 1533–1546 (2012).
[29] L. M. Martinez and C. A. Angell, Nature **410**, 663–667 (2001).
[30] M. Salinga, E. Carria, A. Kaldenbach, M. Bornhöfft, J. Benke, J. Mayer, and M. Wuttig, Nat. Commun. **4**, 2371 (2013).
[31] T. Ozawa, J. Therm. Anal. Calorim. **2**, 301–324 (1970).
[32] T. Ozawa, Polymer (Guildf). **12**, 150–158 (1971).
[33] R. Svoboda, M. Krbal, and J. Málek, J. Non. Cryst. Solids **357**, 3123–3129 (2011).
[34] R. Svoboda and J. Málek, J. Therm. Anal. Calorim. **111**, 161–171 (2012).
[35] A. A. Elabbar and A. A. Abu-Sehly, Mater. Chem. Phys. **141**, 713–718 (2013).
[36] A. El-Korashy, H. El-Zahed, M. Radwan, and A. M. Abdalla, Thin Solid Films **261**, 328–333 (1995).

[37]J. C. Mauro and A. K. Varshneya, Phys. Status Solidi **242**, R46–R48 (2005).
[38]T. Takahashi, K. Murano, K. Nagata, and Y. Miyamoto, Phys. Rev. B **28**, 4893–4895(R) (1983).
[39]Y. Miyamoto, Jpn. J. Appl. Phys. **19**, 1813–1819 (1980).
[40]P. Boolchand and P. Suranyi, Phys. Rev. B **7**, 57–60 (1973).
[41]See supplementary material at http://dx.doi.org/10.1063/1.4886185 for ultrafast DSC calibration, thermal lag analysis and additional SEM and ultrafast DSC results on SeTe flakes deposited on the ultrafast DSC sensor chips.